Geophysical Research Letters

RESEARCH LETTER
10.1029/2025GL120326

Layered Seismic Anisotropy and Tectonics of the Anatolian Plate

Chuanming Liu[1,2], Vera Schulte-Pelkum[3,4], Thorsten W. Becker[2,5], Frederik Link[6,7], and Lili Feng[8]

[1]Department of Geological Sciences, University of Missouri Columbia, Columbia, MO, USA, [2]Institute for Geophysics & Department of Earth and Planetary Sciences, Jackson School of Geosciences, The University of Texas at Austin, Austin, TX, USA, [3]Cooperative Institute for Research in Environmental Sciences, University of Colorado Boulder, Boulder, CO, USA, [4]Department of Geological Sciences, University of Colorado Boulder, Boulder, CO, USA, [5]Oden Institute for Computational Engineering & Sciences, The University of Texas at Austin, Austin, TX, USA, [6]Department of Earth and Planetary Sciences, Yale University, New Haven, CT, USA, [7]Institute of Geosciences, Johannes Gutenberg University Mainz, Mainz, Germany, [8]Pinterest, San Francisco, CA, USA

Abstract Anatolian tectonics are associated with slab retreat in the west and gravitational potential energy and continental collision in the east, leading to westward motion of Anatolia relative to Eurasia, partially accommodated on the North and East Anatolian transform faults. We construct a three-layer, azimuthal seismic anisotropy model using new Rayleigh wave measurements and compare results against geodetic strain-rates and new receiver function analysis for the crust, as well as new and existing shear wave splitting for the mantle to link surface and deep dynamics. In the crust, anisotropy is primarily controlled by recent tectonics, especially along major fault zones. In the lithospheric mantle, anisotropy reflects ongoing tectonic deformation in western Anatolia, whereas eastern Anatolia mainly preserves prior deformation signatures. In the asthenosphere, anisotropy reflects mantle convection, including the effects of Hellenic slab retreat. Our model provides new constraints on lithospheric deformation and geodynamics in the Eastern Mediterranean.

Plain Language Summary The speed of seismic waves depends on the direction of travel, a phenomenon known as seismic anisotropy. This property reflects the alignment of structural fabrics formed during deformation in the lithosphere and asthenosphere, helping us infer tectonic history and mantle flow. Here, we construct a new 3-D model of seismic azimuthal anisotropy for Anatolia. Fast orientations in most of the crust record geologically recent deformation along the major strike-slip faults, the anisotropy in the deeper mantle lithosphere reflects past tectonics, and anisotropy in the asthenosphere reveals current mantle convection patterns. These findings highlight the layered nature of deformation and the lithospheric memory of past deformation in plate boundary regions dominated by large-scale transtensional tectonics.

Key Points:

- A new azimuthally anisotropic model of Anatolia is constructed using surface waves, shear wave splitting, and receiver functions
- Crustal anisotropy near major transform faults reflects transtension, while deeper anisotropy reflects asthenospheric convection
- Layered anisotropy records recent crustal strain, inherited lithospheric fabrics, and ongoing slab-influenced mantle flow

Supporting Information:

Supporting Information may be found in the online version of this article.

Correspondence to:

C. Liu,
chuanming.liu@missouri.edu

Citation:

Liu, C., Schulte-Pelkum, V., Becker, T. W., Link, F., & Feng, L. (2026). Layered seismic anisotropy and tectonics of the Anatolian plate. *Geophysical Research Letters*, *53*, e2025GL120326. https://doi.org/10.1029/2025GL120326

Received 12 NOV 2025
Accepted 17 MAR 2026

Author Contributions:

Conceptualization: Chuanming Liu, Vera Schulte-Pelkum, Thorsten W. Becker
Data curation: Chuanming Liu, Lili Feng
Formal analysis: Chuanming Liu, Vera Schulte-Pelkum, Thorsten W. Becker, Frederik Link
Investigation: Chuanming Liu
Methodology: Chuanming Liu, Vera Schulte-Pelkum, Frederik Link
Visualization: Chuanming Liu
Writing – original draft: Chuanming Liu
Writing – review & editing: Chuanming Liu, Vera Schulte-Pelkum, Thorsten W. Becker, Frederik Link, Lili Feng

1. Introduction

The Anatolian lithosphere in the Eastern Mediterranean is driven and deformed by a range of tectonic processes, including active slab rollback along the Hellenic subduction zone in the west and continental collision between the Arabian and Eurasian Plates in the east (e.g., Royden & Faccenna, 2018; Şengör et al., 1985, 2005). These forcings lead to the westward extrusion of the Anatolian Plate, accommodated by large-scale transtensional deformation along the North Anatolian Fault (NAF) and East Anatolian Fault (EAF) (e.g., Armijo et al., 1999; Hubert-Ferrari et al., 2002). While the broad tectonics and kinematics of the Anatolian Plate are now relatively well established, the coupling between crustal, lithospheric, and asthenospheric deformation and the role of mantle convection in shaping the observed surface kinematics remains poorly understood.

Seismic anisotropy denotes the propagation or polarization dependence of wave speeds; its inference is a key tool for studying lithospheric deformation as it provides an estimate of evolving tectonic regimes at depth (e.g., Biryol et al., 2010; Endrun et al., 2011; Faccenna et al., 2014; Le Pichon & Kreemer, 2010; Link & Rümpker, 2023; Paul et al., 2014). As a result of mantle convection, deep seismic anisotropy develops through the formation of a crystallographic preferred orientation (CPO) of intrinsically anisotropic minerals such as olivine. Particularly, crustal anisotropy is also expected to show contributions from shape-preferred orientation (SPO) and encompasses lithologically distinct fabrics, melt, or cracks. Both mechanisms depend on strain, allowing anisotropy to record lithospheric deformation and mantle flow, albeit sometimes in non-unique ways.

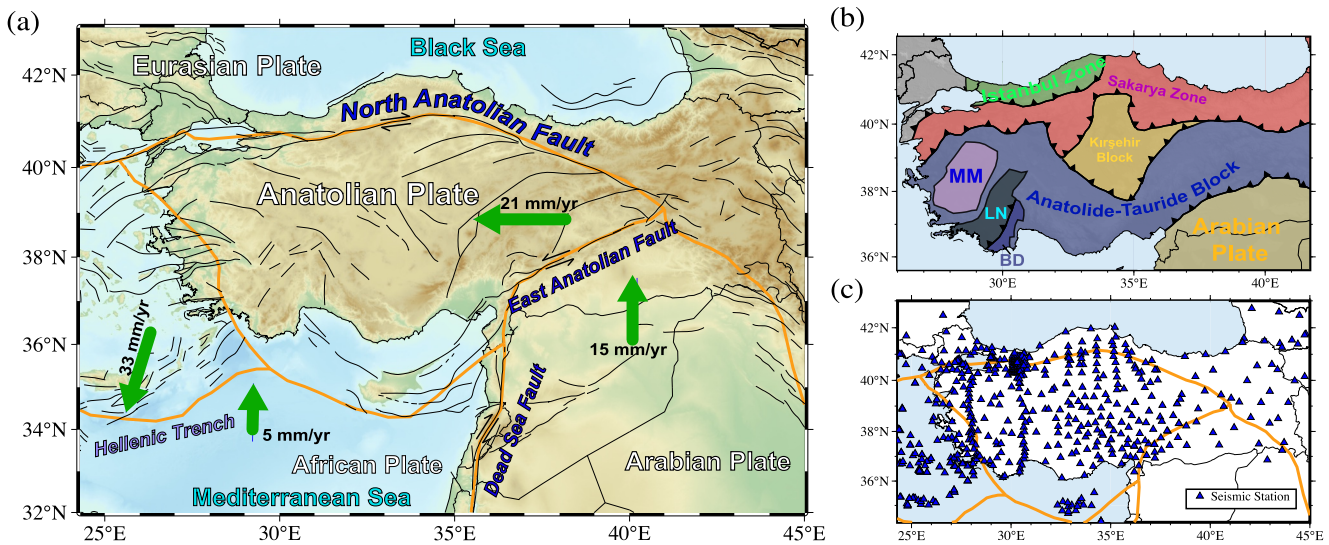

Figure 1. (a) Tectonic setting of the eastern Mediterranean. Black lines denote major faults (Barrier et al., 2004). Green arrows represent plate motion velocities with respect to Eurasia from Reilinger et al. (2006). Orange lines represent the plate boundaries (Bird, 2003). (b) Simplified map of geological terranes of the eastern Mediterranean. MM: Menderes Massif, LN: Lycian Nappes, BD: Bey Dağları (after Okay & Tüysüz, 1999; van Hinsbergen et al., 2010). (c) Distribution of utilized seismic stations in the study region (blue triangles). The full station distribution is illustrated in Figure S1 of Supporting Information S1.

Benefiting from the deployment of an increased set of broadband seismometers, several recent studies inferred seismic anisotropy for Anatolia at different scales and using different seismic wave types. For example, Keles et al. (2024) inferred layered anisotropy from receiver functions for the western NAF. Wang et al. (2020) constructed a crustal *P*-wave anisotropy model with local earthquakes. Al-Lazki et al. (2004) and Mutlu and Karabulut (2011) used *Pn* waves to study anisotropy near the Moho, and Wei et al. (2019) constructed a 3-D *P*-wave anisotropy model down to ∼1,100 km. Legendre et al. (2021) reported anisotropic Rayleigh wave phase velocity maps across Anatolia. Many have used the depth-integrated anisotropy inferred from shear-wave splitting of teleseismic phases to investigate anisotropy and mantle dynamics across Anatolia and the Eastern Mediterranean (e.g., Biryol et al., 2010; Lynner et al., 2022; Sandvol et al., 2003), including using regional two-layer estimates (e.g., Erman et al., 2022; Merry et al., 2021) and splitting intensity tomography (Erman et al., 2025).

However, a comprehensive, 3-D, depth-dependent seismic anisotropy model across Anatolia, including the crust, has not yet been fully established, despite its importance for systematically revealing lithospheric deformation in this complex tectonic setting.

Here, we construct a new Rayleigh wave dispersion database using two- and three-station ambient noise interferometry and earthquake data. We invert these measurements for a three-layer upper mantle model to resolve azimuthally anisotropic features from the crust to the asthenosphere. We also analyze a number of stations for crustal anisotropy from receiver functions, conduct a new two-layer shear-wave splitting analysis, and then investigate the coherence between anisotropy and present-day surface deformation, fossil lithospheric signatures, and mantle flow. Our results provide new insights into distributed lithospheric deformation in this tectonically complex region.

2. Data and Methods

2.1. Surface Wave Data and Phase Velocity Maps

We construct a Rayleigh wave phase speed dispersion database for periods of 8–80 s following the approach of Liu et al. (2022). Measurements are obtained from two- and three-station ambient noise interferometry as well as from teleseismic events recorded at broadband seismic stations across Anatolia and the surrounding areas. Stations outside the study region are used as source stations for ambient noise tomography. In total, 1,341 broadband seismic stations are used (Figure S1 in Supporting Information S1), including ∼560 stations within the study area (Figure 1c). The time range for both ambient noise and earthquake events spans 2005 to 2020, and 2758 teleseismic events with $Ms > 5$ that occurred during that period are used (Figure S2 in Supporting Information S1).

The ambient noise data processing follows Bensen et al. (2007). Rayleigh wave phase speed measurements are obtained using automatic frequency-time analysis (FTAN, e.g., Levshin & Ritzwoller, 2001) for two- and three-station ambient noise and earthquake data. Three-station interferometry improves the signal-to-noise ratio and connects asynchronous station pairs (Zhang et al., 2020), which is important for resolving azimuthal anisotropy (Liu et al., 2022; Zhang et al., 2021). The number of dispersion measurements as a function of period is shown in Figure S3 in Supporting Information S1.

The local isotropic Rayleigh wave phase speed and azimuthal anisotropy are directly estimated on a 0.2° by 0.2° grid using eikonal tomography (Lin et al., 2009) for ambient noise data (8–50 s) and Helmholtz tomography (Lin & Ritzwoller, 2011a) for earthquake data (28–80 s). To improve the robustness of azimuthal anisotropy estimates in Rayleigh-wave phase velocities, we apply azimuthal stacking and binning following Liu et al. (2022), yielding a spatial resolution of ∼1.2° for azimuthal anisotropy. Figure S4 in Supporting Information S1 shows examples of the binned Rayleigh-wave phase velocity measurements, and the azimuthal coverage for all grid points is shown in Figure S5 of Supporting Information S1.

For a given frequency, the local Rayleigh wave phase speed, c, in a weakly anisotropic medium for a wave propagating at azimuth ψ can be approximated by 2ψ (180° periodic) anisotropy and apparent 1ψ anisotropy (e.g., Lin & Ritzwoller, 2011b; Smith & Dahlen, 1973):

$$c(\psi) = c_{\text{iso}} + \delta c_{\text{AA}}(\psi) \approx c_{\text{iso}}\left(1 + \frac{A_1}{2}\cos\left(\psi - \psi_1\right) + \frac{A_2}{2}\cos\left(2\left(\psi - \psi_2\right)\right)\right). \quad (1)$$

Here, c_{iso} is the isotropic phase speed, δc_{AA} is the azimuthal anisotropy perturbation, ψ_1 and ψ_2 are the fast propagation orientations ("fast axes"), and A_1 and A_2 are the peak-to-peak relative amplitudes for 1ψ and 2ψ, respectively. The 1ψ contributions are typically strong at long periods (>50 s) and are not caused by intrinsic anisotropy, but by effects such as scattered body-wave interference (Zeng et al., 2024). To reduce non-intrinsic 1ψ bias at long periods (>50 s, only earthquake data), we resolve both 1ψ and 2ψ anisotropy simultaneously, while accounting for finite-frequency effects through Helmholtz tomography. Strong 1ψ signals are found in the northeast of our study region at 50 s and along the western margin of Anatolia at 70 and 80 s (Figure S6 in Supporting Information S1). However, we focus our analysis on the 2ψ terms here.

Uncertainties in c_{iso} and δc_{AA} are obtained by fitting Equation 1 to binned observations from both ambient noise and earthquake measurements. We directly use the Rayleigh wave phase velocity c_{iso} and its 2ψ azimuthal anisotropy (ψ_2 and A_2) and corresponding uncertainties. Our Rayleigh wave phase velocity and azimuthal anisotropy maps are shown in Figure S7 of Supporting Information S1.

In the eastern margin of Anatolia, the inter-station distances are much larger than those in the rest of the study region (Figure S8 in Supporting Information S1). For this area, we use only the shorter periods (<55 s) from both ambient noise and earthquakes, as the Helmholtz tomography may not be stable in the region with sparse station spacing and limited long period data. This region is also marked in Figures 2c, 3e, and 3f to indicate the relatively poorly constrained regions in the asthenosphere.

2.2. Surface Wave Inversion Method

The isotropic and anisotropic parts of the Rayleigh wave phase velocity are decomposed using both eikonal and Helmholtz tomography. A two-step inversion procedure is applied to resolve depth-dependent shear wave speed and shear wave azimuthal anisotropy, following Liu, Sheehan, and Ritzwoller (2024) and Liu, Becker, et al. (2024).

First, we employ a Bayesian Monte Carlo inversion to invert for a 3-D isotropic V_{SV} model from a set of local 1-D isotropic V_{SV} profiles on a 0.4° by 0.4° grid across the study region. Each 1-D isotropic V_{SV} model is inverted from the Rayleigh wave isotropic phase velocity data at each grid. The parameterization for the 1-D *Vs* model at each grid follows Feng and Ritzwoller (2019), with three layers: sediment, crystalline crust, and upper mantle. The Moho depth is fixed using constraints from receiver functions (Ogden & Bastow, 2021). The prior constraints are summarized in Table S1 of Supporting Information S1, and an example of the posterior parameter distribution is shown in Figure S9 of Supporting Information S1. The inverted sedimentary thickness and the Moho depth map used in this study are shown in Figure S10 of Supporting Information S1. The resulting isotropic model is used to calculate the sensitivity kernels for the next step.

We then invert the Rayleigh wave phase velocity anisotropy (8–80 s) for depth-dependent shear wave azimuth anisotropy at each grid point and combine the individual results into a model of 3-D azimuthal anisotropy. Azimuthal anisotropy is parameterized with three layers: (a) crystalline crust layer (from the bottom of sediments to the Moho), (b) lithospheric mantle layer (a 40 km thick layer beneath the Moho), and (c) asthenospheric layer extending from the base of the lithosphere (LAB) to 200 km depth. Sedimentary layers are treated as isotropic because they lack constraints. Our choice of lithospheric mantle thickness is based on the LAB estimates of Kind et al. (2015). However, we also tested the influence of a thicker lithosphere, which mainly affects the relative amplitudes but not the fast orientations of anisotropy in the two bottom layers (Text S1 in Supporting Information S1). This layered structure is based on the variations in the fast orientation patterns of the Rayleigh phase velocity with period (Figure S7 in Supporting Information S1), and an example of the variation in the fast orientation with period is shown in Figure S11b of Supporting Information S1.

We use a Bayesian Monte Carlo method (Liu, Becker, et al., 2024; Liu, Sheehan, & Ritzwoller, 2024) to invert Rayleigh wave phase speed azimuth anisotropy (ψ_2, A_2) measurements for depth-dependent azimuthal anisotropy (ϕ_{SV}, A_{SV}), with more details provided in Text S2 of Supporting Information S1. The lateral resolution of the final azimuthal anisotropy model is primarily controlled by the smoothing applied during the tomographic step, and is of the order of ∼120 km. The uncertainties in the azimuthal anisotropy variables (ϕ_{SV}, A_{SV}) are estimated from one standard deviation of the posterior distribution, the corresponding uncertainty maps are shown in Figure S12 in Supporting Information S1. An example of the inversion at a grid point is shown in Figure S11 in Supporting Information S1.

2.3. Receiver Function Analysis

There have been a range of prior receiver function studies for Anatolia, including regional anisotropy work (e.g., Keles et al., 2024; Licciardi et al., 2018). However, to obtain a uniform set of measurements for plate-scale analysis, we chose to analyze a more complete set of stations.

We use teleseismic events with epicentral distances of 28°–150° and $M > 5.0$ from 2005 to 2020 recorded at the permanent network KO and the temporary networks YL, YH, and YB; some of the additional networks shown in Figure 1c are not used for this analysis because runtimes are shorter than 1 year. Both radial and transverse receiver functions are calculated using the iterative time-domain deconvolution method of Ligorría and Ammon (1999). A Gaussian low-pass filter, $G(\omega) = \exp(-\omega^2/4a^2)$ with a width parameter $a = 3.0$, is applied, corresponding to a low-pass filter of 0.8 Hz. We use automated quality control following Schulte-Pelkum and Mahan (2014) and then extract information about contrasts in seismic anisotropy by combining radial and transverse receiver functions and solving for the first back-azimuthal harmonic, A_1^{RF} (Schulte-Pelkum, Ross, et al., 2020). This approach yields the strike of the plane perpendicular to the symmetry axis (corresponding to the fast orientation for slow-axis symmetry, which is typical for the crust; Brownlee et al., 2017), as well as the amplitude and depth of contrasts in plunging-axis anisotropy.

This approach has been used previously in other settings to image fabric related to faulting (Schulte-Pelkum, Ross, et al., 2020; Schulte-Pelkum et al., 2024), shear layers (Schulte-Pelkum & Kilb, 2024), and volcano-magmatic fabric (Schulte-Pelkum & Haney, 2024), for example. Here, we use the largest arrival per station, $A_{1\,max}^{RF}$, to represent crustal anisotropy (Figures 2d and S13 in Supporting Information S1, with uncertainty shown in Figure S13 in Supporting Information S1). As discussed in Section 3.1, our results differ somewhat from prior work; the comparison between receiver functions and surface wave anisotropy is presented in Section 4.1.

2.4. Shear Wave Splitting Analysis

A range of shear wave splitting (SWS) results is available for the region, and station-averaged splitting is a useful indicator of path-averaged anisotropy (e.g., Biryol et al., 2010; Paul et al., 2014). However, back-azimuthal variations indicative of multi-layer anisotropy have been documented for several stations, particularly along the NAF (e.g., Merry et al., 2021) and in western Anatolia (Erman et al., 2022). To provide independent constraints on shear-wave anisotropy, we therefore also performed new, one- and two-layer SWS analyses.

We analyzed teleseismic XKS phases recorded at 718 stations in the region. For each, earthquakes with Mw ≥ 5.5 and epicentral distances of 89°–140° were selected from the beginning of station operation through August 2022.

Splitting parameters (fast direction ϕ and delay time δt) were determined using SplitRacer (Link et al., 2022) based on transverse energy minimization. To assess depth-dependent anisotropy, we performed joint station-based inversions for both one- and two-layer models following Link and Rümpker (2023). Stations exhibiting systematic back-azimuthal variations were modeled using two horizontal anisotropic layers. Detailed procedures and comparison with results of Merry et al. (2021) are provided in Text S3 of Supporting Information S1. From this, we identify 298 stations for which we obtain plausible two-layer solutions. Comparisons between the one- and two-layer models and surface-wave anisotropy are presented in Section 4.1 and Figures 3c–3f.

3. Results and Interpretation

We focus on fast orientations and amplitudes (ϕ_{SV} and A_{SV}) of azimuthal anisotropy in three layers: the crust, lithospheric mantle, and underlying asthenosphere (Figure 2).

Figure 2 shows two striking first-order features. First, the surface wave crustal fast orientations are mostly not parallel to the major transform faults (NAF and EAF), unlike in other regions (e.g., the San Andreas Fault, Lin et al., 2011; the Denali fault, Feng et al., 2020). This contrasts with the strikes derived from receiver functions (Figure 3a), which tend to be parallel to local faults. Second, the surface wave data require a three-layer model with a significant change in orientation between the lithosphere, the crust, and the asthenosphere across large parts of the study area; that is, they are not well fit by a two-layer model (Figure S11 in Supporting Information S1). We discuss potential causes for these observations below.

3.1. Crust

For our surface wave crustal anisotropy model (Figure 2a), the sensitivity is mainly to the lower crust, constrained by the shortest period of the ambient noise data. In northern Anatolia and along the NAF, the fast orientations are consistently NE-SW and oblique to the strike of the NAF. In western Anatolia, the fast orientations rotate toward ENE-WSW, possibly influenced by the extensional deformation associated with the rollback of the Hellenic slab. The azimuthal anisotropy amplitude is relatively low around the Lycian Nappes (LN, see Figure 1a), possibly due to shallow layering of carbonate platform rocks and metamorphic rocks (e.g., van Hinsbergen et al., 2010). In central Anatolia, current surface strain rates are low (e.g., Le Pichon & Kreemer, 2010; Weiss et al., 2020), and seismicity is relatively subdued (Tan et al., 2008). Azimuthal anisotropy may be dominated by fossil CPO and local fault fabric.

In the central Anatolide-Tauride Block (ATB) (30°E–32°E) and western Kırşehir Block (KB), fast orientations show an NW-SE pattern, matching local fault strikes. In the central KB, seismic azimuthal anisotropy also shows a weak amplitude, possibly due to gently dipping foliations of the metamorphic domes of the Central Anatolian Crystalline Complex (e.g., Whitney et al., 2001). For the eastern part of the ATB (32°E–40°E), the fast orientations rotate from NE–SW to nearly E–W across the EAF. A detailed analysis of crustal azimuthal anisotropy and crustal deformation and their relationship with the North and East Anatolian Faults is presented in Section 4.

Receiver function results (Figure 2d) show strikes that are primarily parallel to fault traces and show higher amplitudes in the vicinity of faults. $A^{RF}_{1\ max}$ depths are dominantly in the upper to middle crust (0–20 km). Amplitudes tend to be larger at stations close to surface fault traces, and strikes tend to be parallel to nearby fault traces. Station profiles from the temporary experiment crossing the NAF near its northern apex show rotation of the strike to fault-parallel at stations near the NAF, as well as an increase in amplitude toward the fault on some of the station lines. The results are similar to but appear more internally consistent than those of Licciardi et al. (2018) for this region. At a denser array crossing a branching section of the western NAF (Figure 2d, zoom in Figure S13 of Supporting Information S1), strikes near fault traces are fault-parallel at some sites and oblique at others, with the region between the two branches exhibiting oblique strikes from upper to midcrustal depths. Our imaged receiver function anisotropy strikes are dissimilar to those inferred by Keles et al. (2024).

3.2. Lithospheric Mantle

The fast orientations in this layer of our surface wave model (Figures 2b and S14 in Supporting Information S1) change markedly from the crustal pattern, especially for the ATB. This indicates spatially or temporally decoupled deformation between the crust and the lithospheric mantle, or changes in mineralogy (e.g., Bernard & Behr, 2017) or fabric type (e.g., Bernard et al., 2019, 2021). In western Anatolia (26°E–30°E), the fast orientations

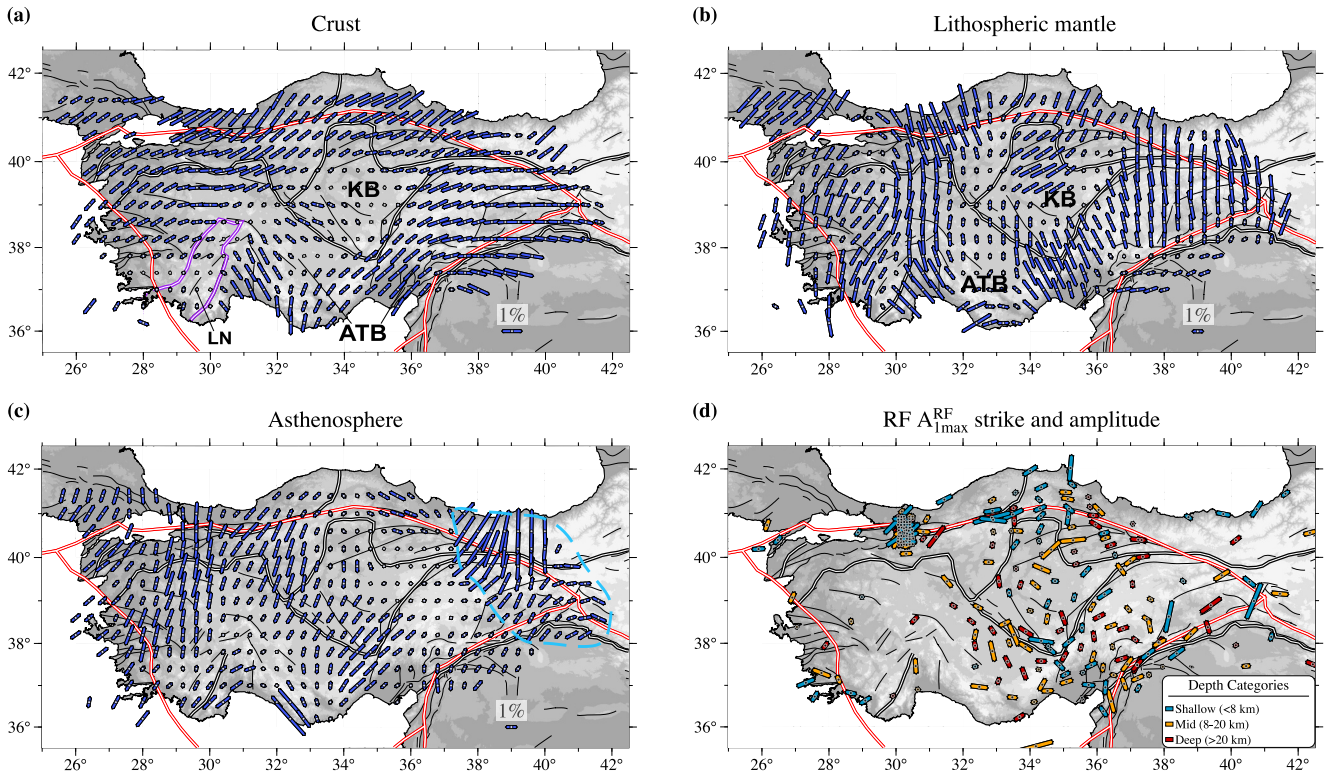

Figure 2. Azimuthal anisotropy across Anatolia inferred from surface waves for the (a) crust, (b) lithospheric mantle, and (c) asthenosphere. The blue bars indicate fast propagation orientations at each depth, with lengths proportional to the anisotropy amplitude. KB: Kırşehir Block; LN: Lycian Nappes; ATB: Anatolide-Tauride Block (Figure 1b). The purple outline delineates the Lycian Nappe in (a). The red lines indicate major plate boundaries. The white lines represent suture zones (from Okay & Tüysüz, 1999). Thin black lines represent local faults. The light-blue polygon in (c) marks the region in the asthenosphere with a relatively long inter-station distance and low confidence. (d) Azimuthal anisotropy strike and amplitude derived from receiver function $A^{RF}_{1\ max}$ observations. The colored bars indicate receiver function $A^{RF}_{1\ max}$ strike, with lengths proportional to the anisotropy amplitude and colors representing the depth of the $A^{RF}_{1\ max}$ conversion (see the legend). The black box outlines the region with a dense array; the result for the zoomed-in region is shown in Figure S13 of Supporting Information S1.

are ENE. The central (30°E–32°E) and eastern (36°E–40°E) parts of Anatolia show roughly N-S orientations. The roughly N-S pattern at 30°E–32°E and 38°E–40°E has also been found in *P*-wave anisotropic tomography at 60 km depth (Wei et al., 2019) and splitting intensity tomography at 70 km depth (Erman et al., 2025).

Erman et al. (2025) proposed that the N-S oriented anisotropy in eastern Anatolia at 70 km depth could be related to the southward flow of asthenospheric material (cf. Faccenna et al., 2006, 2014; Lynner et al., 2022) replacing thinned or detached mantle lithosphere. Another possible reason for the pattern of seismic anisotropy in the lithosphere is inherited anisotropy, which may reflect prior lithospheric compressional deformation in the amalgamation process of the Anatolian Plate since 80 Ma (e.g., van Hinsbergen et al., 2020).

The fast orientation pattern differences among the three layers in eastern Anatolia (Figure S14 in Supporting Information S1) show that the lithospheric mantle pattern differs from that of the asthenosphere, and such distinct fossil anisotropy has been suggested elsewhere in the region (e.g., Endrun et al., 2011; Legendre et al., 2021). The boundary between the different orientations of anisotropy also approximately aligns with the suture zone between the KB and ATB, suggesting inheritance of different NNW and N-S patterns in the western and eastern ATB and the ENE pattern in the KB.

3.3. Asthenosphere

Asthenospheric anisotropy is expected to be governed by mantle convection. The imaged azimuthal anisotropy in the asthenosphere is shown in Figure 2c. For the large regional-scale patterns, fast orientations are NNE across most of western Anatolia and NE in the eastern ATB. While these orientations are broadly consistent with a

northeastward or toroidal flow component, the spatial variability of the fast orientations across Anatolia suggests that a single, uniform asthenospheric flow model is insufficient (cf. Faccenna et al., 2014). Localized flow perturbations driven by slab fragmentation, tears, and the interaction between the Aegean and Cyprus subduction segments, for example, may contribute to the observed heterogeneity.

The uncertainty in the asthenosphere is generally larger than that for the first two layers (Figure S12 in Supporting Information S1), for two reasons: First, in our model parameterization, this layer lies mostly below 100 km and is constrained primarily by long-period teleseismic earthquake data alone, which have much larger uncertainty in measurements than the short periods constrained by the ambient noise. Second, the vertical resolution for depths greater than 100 km is limited by broader sensitivity kernels at long periods. The relatively high uncertainty in the asthenosphere in the eastern margin of Anatolia arises from the use of shorter periods (<50 s), necessitated by limited data coverage. To test the robustness of the fast orientations of the third layer, we compare our results with SWS in Section 4.

4. Discussion

4.1. Comparison With Other Seismic Observations

Receiver function (RF) analysis and shear wave splitting (SWS) provide complementary constraints on seismic anisotropy, each with a distinct sensitivity and resolution. For comparison, we interpolate the surface-wave (SW) anisotropy model to the station locations with RF and SWS measurements and analyze only those stations that are located near SW anisotropy grid points with sufficiently large anisotropy amplitudes (>0.3%) and small azimuthal uncertainties (<35°).

Receiver functions can constrain *P*-wave anisotropy contrasts beneath stations in dipping foliation (e.g., Park & Levin, 2016; Schulte-Pelkum & Mahan, 2014). As shown in Figure 3a, the fast orientations of crustal anisotropy from the surface waves exhibit a more homogeneous pattern, whereas those from receiver functions display more localized variations, as might be expected. Receiver function $A_{1\,\max}^{\mathrm{RF}}$ can achieve a horizontal resolution of ∼20 km at Moho depths to a few km in the shallow crust, which is much higher than the ∼120 km resolution of the surface wave anisotropy model.

Compared with the surface wave crustal anisotropy, the receiver function $A_{1\,\max}^{\mathrm{RF}}$ yields more fault-strike-parallel orientations, especially along the North and East Anatolian Faults. The mean angular difference between the two data sets is 38°, indicating relatively low coherence (45° being random for angular deviations in [0°, 90°]). Besides the difference in lateral resolution, receiver function $A_{1\,\max}^{\mathrm{RF}}$ captures the maximum anisotropic contrast at variable depths, whereas surface wave anisotropy primarily reflects bulk lower crustal properties. Similar discrepancies between surface wave and receiver function anisotropy have been reported in southern California (Schulte-Pelkum et al., 2021) and Alaska (Feng et al., 2020; Schulte-Pelkum, Caine, et al., 2020). Thus, receiver function anisotropy can complement surface wave anisotropy, but a joint inversion for a complete anisotropy model that accounts for imaging differences would provide further insights into strike-slip regions.

The two-layer shear-wave splitting (SWS) model is compared with our surface-wave (SW) three-layer model at 128 stations (Figures 3c–3e). For the upper layer of the SWS model, 49% of the stations show an angular difference of less than 20° relative to the SW crustal layer, mainly concentrated near the NAF and EAF (Figure 3c). In contrast, 23% of the stations are more consistent with the SW lithospheric layer, primarily in northwestern and central Anatolia. The regionalization maps for this comparison are shown in Figure S16 of Supporting Information S1.

For the lower SWS layer, the fast orientations agree well with the SW asthenospheric layer at stations in northwestern and central Anatolia (Figure 3e). In contrast, along the plate boundaries, including some segments of the eastern EAF and the eastern NAF, the lower SWS layer shows better agreement with the SW lithospheric layer (Figure 3d; Figure S16b in Supporting Information S1). This comparison helps constrain the depth origin of anisotropy inferred from the two-layer SWS analysis. It also demonstrates that both the crust and mantle lithosphere can generate significant anisotropic signals in the SWS observations, particularly along the NAF and EAF.

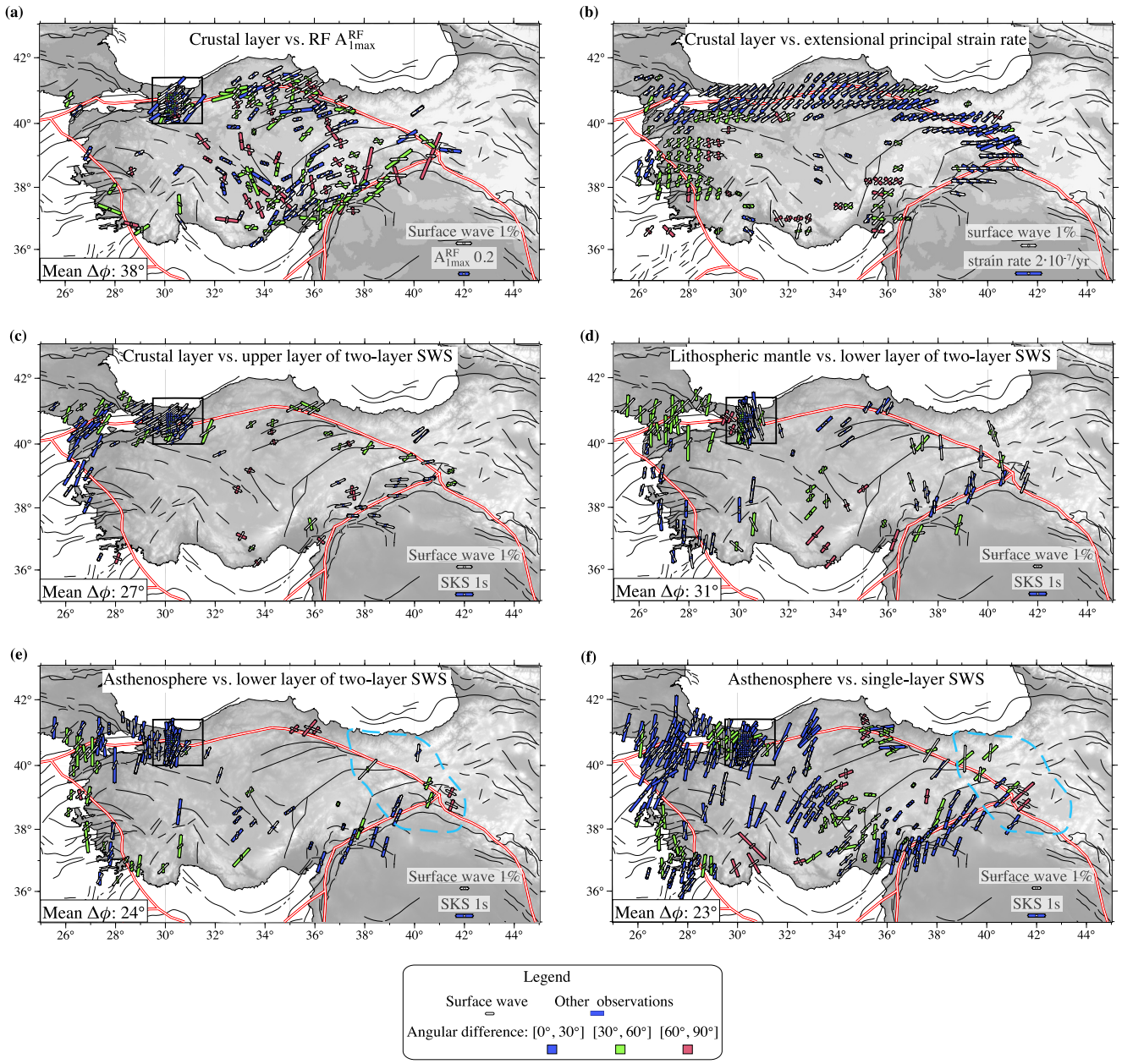

Figure 3. Comparison of fast orientations from our surface wave azimuthal anisotropy model with independent observations, including receiver function $A^{RF}_{1\,max}$, geodetically inferred strain rates, and shear wave splitting (SWS) fast axes. (a) White bars show surface wave anisotropy in the crustal layer, and colored bars denote receiver functions, $A^{RF}_{1\,max}$, color-coded by angular differences relative to the surface wave results. The mean angular difference ($\Delta\phi$) is shown in the lower-left corner; red lines indicate plate boundaries. The black box outlines the dense array region, with corresponding zoomed-in maps shown in Figure S15 of Supporting Information S1. (b) Same as (a), but for the surface wave crustal layer compared with the maximum extensional principal strain rate directions derived from geodetic constraints (Weiss et al., 2020). (c) Same as (a), but for the surface wave crustal layer compared with the upper layer of the two-layer SWS model. (d) Same as (a), but for the surface wave lithospheric mantle layer compared with the lower layer of the two-layer SWS model. (e) Same as (a), but for the surface wave asthenosphere compared with the lower SWS layer. (f) Same as (e), but for the surface wave asthenosphere compared with our single-layer SWS model, which has broader station coverage than the two-layer case. The light-blue polygon in (e, f) marks the region of reduced confidence in the asthenosphere due to large interstation spacing.

The single-layer SWS model is easier to invert for and is compared with the lithospheric and asthenospheric layers of our SW model at a larger set of 295 stations (Figure 3f). The SWS fast orientations are generally consistent with the SW asthenospheric layer across most of western, central, and southeastern Anatolia. Compared with the SW lithospheric layer, the SWS fast orientations show good agreement in the southwestern and central-northern

regions, as well as in areas where the fast orientations are similar in both the lithospheric and asthenospheric layers (Figure S17a in Supporting Information S1).

Overall, our inferences on asthenospheric anisotropy are consistent with the single-layer SWS model and the lower layer of the two-layer SWS model in most of the study region.

The comparison between our SW three-layer model and the single- and two-layer SWS models allows us to identify the dominant sources of anisotropy for most SWS observations under both configurations. However, significant angular discrepancies occur in the northeastern NAF region when both the single- and two-layer SWS models are compared with the SW model layers. These mismatches coincide with areas of relatively poor data coverage.

4.2. Crustal Azimuthal Anisotropy and Surface Deformation

To better understand crustal azimuthal anisotropy, we also compared our surface wave model with crustal strain rate fields derived from geodesy (Weiss et al., 2020). Figures 3b and S17b in Supporting Information S1 show a comparison between the fast orientations of crustal anisotropy and the orientations of the extensional principal strain rates ($\dot{\varepsilon}_1$) and maximum shear strain rates (cf. Biryol et al., 2010; Le Pichon & Kreemer, 2010). Regions with strain rates below a defined threshold were excluded to avoid overinterpreting small strain regions. Strain rates are high along the NAF, the eastern segment of the EAF, and in western Anatolia, whereas central Anatolia exhibits minimal deformation (e.g., Faccenna et al., 2014; Le Pichon & Kreemer, 2010; Weiss et al., 2020). In western Anatolia (west of 29°E), the seismic anisotropy fast orientations align well with the maximum shear strain rate directions (Figure S17b in Supporting Information S1), indicating large lower-crustal strain rates that dominate CPO development.

Our crustal anisotropy fast orientations agree well with the $\dot{\varepsilon}_1$ orientations along both the NAF and EAF, where the strain rate is significant (Figure 3b). The NAF is a major transform fault that accommodates right-lateral shear between the Eurasian and Anatolian plates and represents one of the Earth's younger strike-slip plate boundaries (e.g., Şengör et al., 2005). The NAF has accrued ∼85 km of total slip (Hubert-Ferrari et al., 2002), which is relatively small compared with other large strike-slip faults, perhaps indicating only moderate strain localization within a nascent shear zone at depth. Our crustal model primarily reflects lower crustal features due to the 8s minimum usable period. The agreement between the fast anisotropy orientations and extension axes thus suggests that the CPO type anisotropy within a broad region away from the NAF and EAF, as imaged by our study, is influenced by relatively small strains in the lower crust, since we would expect successive rotation from $\dot{\varepsilon}_1$ into the shear plane for higher strains (e.g., Zhang & Karato, 1995).

Previous studies have also reported deviations between the fast orientations of seismic anisotropy and the NAF strike based on single-layer shear-wave splitting (e.g., Biryol et al., 2010; Faccenna et al., 2014), which relate upper-mantle anisotropy to large-scale mantle flow. Merry et al. (2021) used two-layer SWS models and reported the fast direction in the upper layer parallel to the strike of the NAF near 28°–30°E and parallel to $\dot{\varepsilon}_1$ orientations in the eastern and western end of the NAF, likewise attributing the rotation of CPO-derived fast orientations to a low-strained mantle shear zone; however, the thickness of the upper layer is poorly constrained. Our surface wave anisotropy model shows a systematic alignment between the fast orientations within the crust and $\dot{\varepsilon}_1$, indicating that transtensional deformation affected CPO in the lower crust away from central shear zones for both the NAF and EAF.

Similar observations have been made along other major strike-slip boundaries, where fast orientations reflect accumulated finite strain rather than simple fault-parallel motion. Beneath the Alpine Fault in the South Island of New Zealand, shear-wave splitting fast orientations deviate from fault strike by approximately 30° in the south, aligning with the direction of maximum finite extension from relatively small accumulated shear (Savage et al., 2004). Similarly, numerical modeling of the San Andreas Fault system suggests that fast orientations in the near-fault lithospheric mantle are approximately fault-parallel, but rotate obliquely with increasing distance, consistent with strain-controlled CPO development as a function of distance from the plate boundary (e.g., Bonnin et al., 2012).

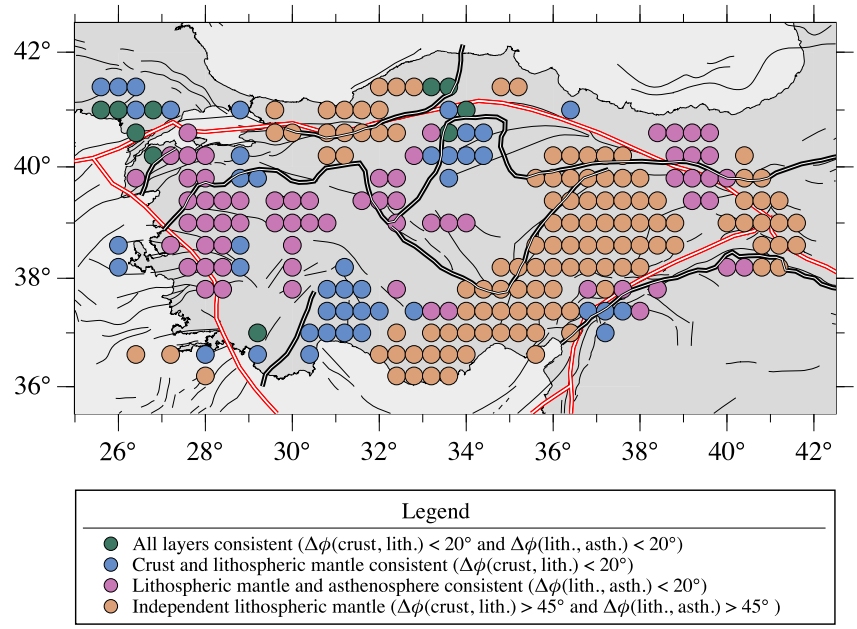

Figure 4. Regionalization map showing the consistency among the three layers based on their angular differences ($\Delta\phi$). Grid points with small anisotropy amplitudes or large uncertainties are masked.

4.3. Depth-Dependent Seismic Anisotropy of Anatolia

Seismic anisotropic studies increasingly employ multi-constraint models to resolve depth-dependent anisotropy (e.g., Endrun et al., 2011; Erman et al., 2025; Legendre et al., 2021; Merry et al., 2021; Wei et al., 2019), but it remains challenging to do so in tectonically complex regions. We find that interactions among subduction, collision, and large-scale transform shear zones (e.g., Faccenna et al., 2006, 2014) have modified the elastic structure of Anatolia from the surface to the upper mantle.

In the crust, the fast orientations along the North Anatolian and East Anatolian Faults align with the extensional principal strain-rate directions as inferred from geodetic constraints. These orientations are mainly associated with distributed shear away from the strike-slip shear zone, whereas fast orientations in western Anatolia are dominated by maximum shear strain directions.

In the lithosphere, fast orientations in western Anatolia gradually change from ENE in the crust to NNE, becoming more like the pattern observed in the asthenosphere (Figure 4). This suggests coupled deformation in which lithospheric strain is affected by underlying mantle flow, partially driven by Hellenic slab rollback. The Anatolide-Tauride Block shows more N-S orientations, and the Kırşehir Block is dominated by ENE orientations, with surface geology as indicated by the suture zone between them clearly separating the azimuthal orientation patterns at depth. The lithospheric anisotropy pattern in both blocks likely reflects the inherited fossil anisotropy from prior tectonics (e.g., van Hinsbergen et al., 2010).

In the asthenosphere, the fast orientations in our model generally align well with those from single-layer and the lower layer of two-layer shear-wave splitting across much of Anatolia, suggesting that strong anisotropy developed with a dominant influence of geologically recent mantle flow. Central and western Anatolia show NE–SW fast orientations, which reflect southwest-directed mantle flow driven by slab rollback.

5. Conclusion

We constructed a 3-D azimuthal seismic anisotropy model of the crust and uppermost mantle of Anatolia based on surface waves and compared it with receiver function and two-layer shear wave splitting analysis. Our model provides a comprehensive view of depth variations in anisotropy. From a cross-scale imaging perspective, surface waves help delineate the depth origin of back-azimuthally dependent shear-wave splitting. While the coherence within the crust from receiver function and surface wave estimates is limited due to different sensitivity, crustal

anisotropy is overall dominated by present-day transform fault zone mechanics, and fast axes align with geodetically constrained maximum extensional strain orientations.

In the lithospheric mantle, anisotropy is regionally variable. Western Anatolia shows coherent deformation between the lithosphere and the deeper mantle associated with recent mantle flow. In contrast, the lithosphere of eastern Anatolia appears dominated by fossil anisotropy. In the asthenosphere, the fast orientations of anisotropy are dominated by recent mantle flow associated with Hellenic slab rollback and other convective patterns.

While anisotropy records the effects of mantle convection on lithospheric deformation and tectonics throughout Anatolia, such depth-variable anisotropy patterns indicate that the crust and mantle lithosphere reflect different deformation episodes. Resolving layered anisotropy is essential for linking surface deformation and fault zone evolution with mantle dynamics in complex plate boundary regions.

Conflict of Interest

The authors declare no conflicts of interest relevant to this study.

Availability Statement

This work incorporates seismic data from FDSN networks. Network details and references are provided in Table S2 of Supporting Information S1. The azimuthal anisotropy models presented herein are available in Liu et al. (2025). We used GMT by Wessel et al. (2019) for our figures.

Acknowledgments
We thank the Editor, Fabio Capitanio, and two anonymous reviewers for their constructive comments, which significantly improved the manuscript. We are grateful to Onur Tan for providing the Turkey earthquake catalog, and to Wei Wei and Eric Sandvol for sharing their seismic models. VSP and TWB were partially supported by NSF Grants EAR-1927246, EAR-1927216, EAR-2049743, and EAR-1853856.

References

Al-Lazki, A. I., Sandvol, E., Seber, D., Barazangi, M., Turkelli, N., & Mohamad, R. (2004). Pn tomographic imaging of mantle lid velocity and anisotropy at the junction of the Arabian, Eurasian and African plates. *Geophysical Journal International*, *158*(3), 1024–1040. https://doi.org/10.1111/j.1365-246x.2004.02355.x

Armijo, R., Meyer, B., Hubert, A., & Barka, A. (1999). Westward propagation of the North Anatolian fault into the northern Aegean: Timing and kinematics. *Geology*, *27*(3), 267–270. https://doi.org/10.1130/0091-7613(1999)027<0267:wpotna>2.3.co;2

Barrier, E., Chamot-Rooke, N., Giordano, G., Morelli, A., & Brouillet, J. F. (2004). *Seismicity and tectonics map of the Mediterranean, scale 1: 10,000,000 at the center of the map*. Commission for the Geological Map of the World.

Bensen, G. D., Ritzwoller, M. H., Barmin, M. P., Levshin, A. L., Lin, F., Moschetti, M. P., et al. (2007). Processing seismic ambient noise data to obtain reliable broad-band surface wave dispersion measurements. *Geophysical Journal International*, *169*(3), 1239–1260. https://doi.org/10.1111/j.1365-246x.2007.03374.x

Bernard, R. E., & Behr, W. M. (2017). Fabric heterogeneity in the Mojave lower crust and lithospheric mantle in Southern California. *Journal of Geophysical Research: Solid Earth*, *122*(7), 5000–5025. https://doi.org/10.1002/2017jb014280

Bernard, R. E., Behr, W. M., Becker, T. W., & Young, D. J. (2019). Relationships between olivine CPO and deformation parameters in naturally deformed rocks and implications for mantle seismic anisotropy. *Geochemistry, Geophysics, Geosystems*, *20*(7), 3469–3494. https://doi.org/10.1029/2019gc008289

Bernard, R. E., Schulte-Pelkum, V., & Behr, W. M. (2021). The competing effects of olivine and orthopyroxene CPO on seismic anisotropy. *Tectonophysics*, *814*, 228954. https://doi.org/10.1016/j.tecto.2021.228954

Bird, P. (2003). An updated digital model of plate boundaries. *Geochemistry, Geophysics, Geosystems*, *4*(3). https://doi.org/10.1029/2001gc000252

Biryol, C. B., Zandt, G., Beck, S. L., Ozacar, A. A., Adiyaman, H. E., & Gans, C. R. (2010). Shear wave splitting along a nascent plate boundary: The North Anatolian fault zone. *Geophysical Journal International*, *181*(3), 1201–1213. https://doi.org/10.1111/j.1365-246x.2010.04576.x

Bonnin, M., Tommasi, A., Hassani, R., Chevrot, S., Wookey, J., & Barruol, G. (2012). Numerical modelling of the upper-mantle anisotropy beneath a migrating strike-slip plate boundary: The San Andreas fault system. *Geophysical Journal International*, *191*(2), 436–458. https://doi.org/10.1111/j.1365-246x.2012.05650.x

Brownlee, S. J., Schulte-Pelkum, V., Raju, A., Mahan, K., Condit, C., & Orlandini, O. F. (2017). Characteristics of deep crustal seismic anisotropy from a compilation of rock elasticity tensors and their expression in receiver functions. *Tectonics*, *36*(9), 1835–1857. https://doi.org/10.1002/2017tc004625

Endrun, B., Lebedev, S., Meier, T., Tirel, C., & Friederich, W. (2011). Complex layered deformation within the Aegean crust and mantle revealed by seismic anisotropy. *Nature Geoscience*, *4*(3), 203–207. https://doi.org/10.1038/ngeo1065

Erman, C., Yolsal-Çevikbilen, S., Eken, T., Huang, Z., & Taymaz, T. (2025). Seismic anisotropy variations in the Eastern Mediterranean Sea region revealed by splitting intensity tomography: Implications on mantle dynamics. *Journal of Geophysical Research: Solid Earth*, *130*(3), e2024JB030331. https://doi.org/10.1029/2024jb030331

Erman, C., Yolsal-Çevikbilen, S., Eken, T., Tilmann, F., Keleş, D., & Taymaz, T. (2022). Constraints on the lithospheric kinematics in the aegean and Western Anatolia unveiled by SKS splitting observations. *Journal of Geophysical Research: Solid Earth*, *127*(12), e2022JB025265. https://doi.org/10.1029/2022jb025265

Faccenna, C., Becker, T. W., Auer, L., Billi, A., Boschi, L., Brun, J. P., et al. (2014). Mantle dynamics in the Mediterranean. *Reviews of Geophysics*, *52*(3), 283–332. https://doi.org/10.1002/2013rg000444

Faccenna, C., Bellier, O., Martinod, J., Piromallo, C., & Regard, V. (2006). Slab detachment beneath eastern Anatolia: A possible cause for the formation of the North Anatolian fault. *Earth and Planetary Science Letters*, *242*(1–2), 85–97. https://doi.org/10.1016/j.epsl.2005.11.046

Feng, L., Liu, C., & Ritzwoller, M. H. (2020). Azimuthal anisotropy of the crust and uppermost mantle beneath Alaska. *Journal of Geophysical Research: Solid Earth*, *125*(12), e2020JB020076. https://doi.org/10.1029/2020jb020076

Feng, L., & Ritzwoller, M. H. (2019). A 3-D shear velocity model of the crust and uppermost mantle beneath Alaska including apparent radial anisotropy. *Journal of Geophysical Research: Solid Earth*, *124*(10), 10468–10497. https://doi.org/10.1029/2019jb018122

Hubert-Ferrari, A., Armijo, R., King, G., Meyer, B., & Barka, A. (2002). Morphology, displacement, and slip rates along the North Anatolian fault, Turkey. *Journal of Geophysical Research*, *107*(B10). https://doi.org/10.1029/2001jb000393

Keleş, D., Eken, T., Licciardi, A., Frederiksen, A. W., & Taymaz, T. (2024). Depth-dependent anisotropy along Northwest segment of the north anatolian fault zone: Evidence for paleo-tectonic structures contributing to overall complexity. *Journal of Geophysical Research: Solid Earth*, *129*(6), e2023JB028014. https://doi.org/10.1029/2023jb028014

Kind, R., Eken, T., Tilmann, F., Sodoudi, F., Taymaz, T., Bulut, F., et al. (2015). Thickness of the lithosphere beneath Turkey and surroundings from S-receiver functions. *Solid Earth*, *6*(3), 971–984. https://doi.org/10.5194/se-6-971-2015

Legendre, C. P., Zhao, L., & Tseng, T.-L. (2021). Large-scale variation in seismic anisotropy in the crust and upper mantle beneath Anatolia. *Turkey. Communications Earth & Environment*, *2*(1), 73. https://doi.org/10.1038/s43247-021-00142-6

Le Pichon, X., & Kreemer, C. (2010). The miocene-to-present kinematic evolution of the eastern Mediterranean and Middle East and its implications for dynamics. *Annual Review of Earth and Planetary Sciences*, *38*(1), 323–351. https://doi.org/10.1146/annurev-earth-040809-152419

Levshin, A. L., & Ritzwoller, M. H. (2001). Automated detection, extraction, and measurement of regional surface waves (pp. 1531–1545). https://doi.org/10.1007/978-3-0348-8264-4_11

Licciardi, A., Eken, T., Taymaz, T., Agostinetti, N. P., & Yolsal-Çevikbilen, S. (2018). Seismic anisotropy in central North Anatolian fault zone and its implications on crustal deformation. *Physics of the Earth and Planetary Interiors*, *277*, 99–112. https://doi.org/10.1016/j.pepi.2018.01.012

Ligorría, J. P., & Ammon, C. J. (1999). Iterative deconvolution and receiver-function estimation. *Bulletin of the Seismological Society of America*, *89*(5), 1395–1400. https://doi.org/10.1785/bssa0890051395

Lin, F., & Ritzwoller, M. H. (2011a). Helmholtz surface wave tomography for isotropic and azimuthally anisotropic structure. *Geophysical Journal International*, *186*(3), 1104–1120. https://doi.org/10.1111/j.1365-246x.2011.05070.x

Lin, F., & Ritzwoller, M. H. (2011b). Apparent anisotropy in inhomogeneous isotropic media. *Geophysical Journal International*, *186*(3), 1205–1219. https://doi.org/10.1111/j.1365-246x.2011.05100.x

Lin, F., Ritzwoller, M. H., & Snieder, R. (2009). Eikonal tomography: Surface wave tomography by phase front tracking across a regional broadband seismic array. *Geophysical Journal International*, *177*(3), 1091–1110. https://doi.org/10.1111/j.1365-246x.2009.04105.x

Lin, F., Ritzwoller, M. H., Yang, Y., Moschetti, M. P., & Fouch, M. J. (2011). Complex and variable crustal and uppermost mantle seismic anisotropy in the western United States. *Nature Geoscience*, *4*(1), 55–61. https://doi.org/10.1038/ngeo1036

Link, F., Reiss, M. C., & Rümpker, G. (2022). An automatized XKS-splitting procedure for large data sets: Extension package for SplitRacer and application to the USArray. *Computers & Geosciences*, *158*, 104961. https://doi.org/10.1016/j.cageo.2021.104961

Link, F., & Rümpker, G. (2023). Shear-wave splitting reveals layered-anisotropy beneath the European alps in response to mediterranean subduction. *Journal of Geophysical Research: Solid Earth*, *128*(9), e2023JB027192. https://doi.org/10.1029/2023jb027192

Liu, C., Becker, T., Wu, M., Han, S., & Ritzwoller, M. H. (2024). Seismic Azimuthal Anisotropy Within the Juan de Fuca - Gorda Plate System. *Geophysical Research Letters*, *51*(22), e2024GL111835. https://doi.org/10.1029/2024gl111835

Liu, C., Schulte-Pelkum, V., Becker, T. W., Link, F., & Feng, L. (2025). Layered seismic anisotropy and tectonics of the anatolian plate (V1.0) [Dataset]. *Zenodo*. https://doi.org/10.5281/zenodo.17306944

Liu, C., Sheehan, A. F., & Ritzwoller, M. H. (2024). Seismic azimuthal anisotropy beneath the Alaska subduction zone. *Geophysical Research Letters*, *51*(14), e2024GL109758. https://doi.org/10.1029/2024GL109758

Liu, C., Zhang, S., Sheehan, A. F., & Ritzwoller, M. H. (2022). Surface wave isotropic and azimuthally anisotropic dispersion across Alaska and the alaska-aleutian subduction zone. *Journal of Geophysical Research: Solid Earth*, *127*(11), e2022JB024885. https://doi.org/10.1029/2022jb024885

Lynner, C., Delph, J. R., Portner, D. E., Beck, S. L., Sandvol, E., & Özacar, A. A. (2022). Slab induced mantle upwelling beneath the anatolian Plateau. *Geophysical Research Letters*, *49*(11), e2021GL097451. https://doi.org/10.1029/2021gl097451

Merry, T. A. J., Bastow, I. D., Kounoudis, R., Ogden, C. S., Bell, R. E., & Jones, L. (2021). The influence of the north anatolian fault and a fragmenting slab architecture on upper mantle seismic anisotropy in the Eastern mediterranean. *Geochemistry, Geophysics, Geosystems*, *22*(9), e2021GC009896. https://doi.org/10.1029/2021gc009896

Mutlu, A. K., & Karabulut, H. (2011). Anisotropic Pn tomography of Turkey and adjacent regions. *Geophysical Journal International*, *187*(3), 1743–1758. https://doi.org/10.1111/j.1365-246x.2011.05235.x

Ogden, C. S., & Bastow, I. D. (2021). The crustal structure of the Anatolian plate from receiver functions and implications for the uplift of the central and eastern Anatolian plateaus. *Geophysical Journal International*, *229*(2), 1041–1062. https://doi.org/10.1093/gji/ggab513

Okay, A. I., & Tüysüz, O. (1999). Tethyan sutures of northern Turkey. *Geological Society, London, Special Publications*, *156*(1), 475–515. https://doi.org/10.1144/GSL.SP.1999.156.01.22

Park, J., & Levin, V. (2016). Anisotropic shear zones revealed by backazimuthal harmonics of teleseismic receiver functions. *Geophysical Journal International*, *207*(2), 1216–1243. https://doi.org/10.1093/gji/ggw323

Paul, A., Karabulut, H., Mutlu, A. K., & Salaün, G. (2014). A comprehensive and densely sampled map of shear-wave azimuthal anisotropy in the Aegean–Anatolia region. *Earth and Planetary Science Letters*, *389*, 14–22. https://doi.org/10.1016/j.epsl.2013.12.019

Reilinger, R., McClusky, S., Vernant, P., Lawrence, S., Ergintav, S., Cakmak, R., et al. (2006). GPS constraints on continental deformation in the africa-arabia-eurasia continental collision zone and implications for the dynamics of plate interactions. *Journal of Geophysical Research*, *111*(B5). https://doi.org/10.1029/2005jb004051

Royden, L., & Faccenna, C. (2018). Subduction orogeny and the late Cenozoic evolution of the Mediterranean Arcs. *Annual Review of Earth and Planetary Sciences*, *46*(1), 261–289. https://doi.org/10.1146/annurev-earth-060115-012419

Ruhr University Bochum. (2007). Nisyros project, RUB bochum, Germany [Dataset]. *GFZ Data Services*. https://doi.org/10.14470/doi-SUFFIX-HERE

Sandvol, E., Turkelli, N., Zor, E., Gok, R., Bekler, T., Gurbuz, C., et al. (2003). Shear wave splitting in a young continent-continent collision: An example from Eastern Turkey. *Geophysical Research Letters*, *30*(24). https://doi.org/10.1029/2003GL017390

Savage, M. K., Fischer, K. M., & Hall, C. E. (2004). Strain modelling, seismic anisotropy and coupling at strike-slip boundaries: Applications in New Zealand and the San Andreas fault. *Geological Society, London, Special Publications*, *227*(1), 9–39. https://doi.org/10.1144/gsl.sp.2004.227.01.02

Schulte-Pelkum, V., Becker, T. W., Behr, W. M., & Miller, M. S. (2021). Tectonic inheritance during plate boundary evolution in southern California constrained from seismic anisotropy. *Geochemistry, Geophysics, Geosystems*, *22*(11), e2021GC010099. https://doi.org/10.1029/2021gc010099

Schulte-Pelkum, V., Bender, A. M., & Ruppert, N. A. (2024). Tectonics and seismic structure of Alaska and Northwestern Canada. *Geophysical Monograph Series*, 575–587. https://doi.org/10.1002/9781394195947.ch21

Schulte-Pelkum, V., Caine, J. S., Jones, J. V., & Becker, T. W. (2020). Imaging the tectonic grain of the Northern Cordillera orogen using transportable array receiver functions. *Seismological Research Letters*, *91*(6), 3086–3105. https://doi.org/10.1785/0220200182

Schulte-Pelkum, V., & Haney, M. M. (2024). Fault–Dike–Magma interactions inferred from transcrustal conical structures under Akutan Volcano. *Seismological Research Letters*, *95*(5), 2663–2673. https://doi.org/10.1785/0220240119

Schulte-Pelkum, V., & Kilb, D. (2024). Lithospheric foundering in progress imaged under an extinct Continental arc. *Geophysical Research Letters*, *51*(24), e2024GL111290. https://doi.org/10.1029/2024gl111290

Schulte-Pelkum, V., & Mahan, K. H. (2014). A method for mapping crustal deformation and anisotropy with receiver functions and first results from USArray. *Earth and Planetary Science Letters*, *402*, 221–233. https://doi.org/10.1016/j.epsl.2014.01.050

Schulte-Pelkum, V., Ross, Z. E., Mueller, K., & Ben-Zion, Y. (2020). Tectonic inheritance with dipping faults and deformation fabric in the brittle and ductile Southern California crust. *Journal of Geophysical Research: Solid Earth*, *125*(8), e2020JB019525. https://doi.org/10.1029/2020jb019525

Şengör, A. M. C., Görür, N., & Şaroğlu, F. (1985). *Strike-slip faulting and related basin formation in zones of tectonic escape: Turkey as a case study* (Vol. 37, pp. 227–264). SEPM Special Publication.

Şengör, A. M. C., Tüysüz, O., İmren, C., Sakinç, M., Eyidoğan, H., Görür, N., et al. (2005). The North Anatolian fault: A new look. *Annual Review of Earth and Planetary Sciences*, *33*(1), 37–112. https://doi.org/10.1146/annurev.earth.32.101802.120415

Smith, M. L., & Dahlen, F. A. (1973). The azimuthal dependence of love and Rayleigh wave propagation in a slightly anisotropic medium. *Journal of Geophysical Research*, *78*(17), 3321–3333. https://doi.org/10.1029/JB078i017p03321

Tan, O., Tapirdamaz, M. C., & Yörük, A. (2008). The earthquake catalogues for Turkey. *Turkish Journal of Earth Sciences*, *17*(2), 405–418.

van Hinsbergen, D. J. J., Torsvik, T. H., Schmid, S. M., Maţenco, L. C., Maffione, M., Vissers, R. L. M., et al. (2020). Orogenic architecture of the Mediterranean region and kinematic reconstruction of its tectonic evolution since the Triassic. *Gondwana Research*, *81*, 79–229. https://doi.org/10.1016/j.gr.2019.07.009

van Hinsbergen, D. J. J., Kaymakci, N., Spakman, W., & Torsvik, T. H. (2010). Reconciling the geological history of western Turkey with plate circuits and mantle tomography. *Earth and Planetary Science Letters*, *297*(3–4), 674–686. https://doi.org/10.1016/j.epsl.2010.07.024

Wang, H., Huang, Z., Eken, T., Keleş, D., Kaya-Eken, T., Confal, J. M., et al. (2020). Isotropic and anisotropic P wave velocity structures of the crust and uppermost mantle beneath Turkey. *Journal of Geophysical Research: Solid Earth*, *125*(12), e2020JB019566. https://doi.org/10.1029/2020jb019566

Wei, W., Zhao, D., Wei, F., Bai, X., & Xu, J. (2019). Mantle dynamics of the Eastern mediterranean and Middle East: Constraints from P-Wave anisotropic tomography. *Geochemistry, Geophysics, Geosystems*, *20*(10), 4505–4530. https://doi.org/10.1029/2019gc008512

Weiss, J. R., Walters, R. J., Morishita, Y., Wright, T. J., Lazecky, M., Wang, H., et al. (2020). High-resolution surface velocities and strain for Anatolia from Sentinel-1 InSAR and GNSS data. *Geophysical Research Letters*, *47*(17), e2020GL087376. https://doi.org/10.1029/2020gl087376

Wessel, P., Luis, J. F., Uieda, L., Scharroo, R., Wobbe, F., Smith, W. H. F., & Tian, D. (2019). The generic mapping tools version 6. *Geochemistry, Geophysics, Geosystems*, *20*(11), 5556–5564. https://doi.org/10.1029/2019gc008515

Whitney, D. L., Teyssier, C., Dilek, Y., & Fayon, A. K. (2001). Metamorphism of the Central Anatolian Crystalline complex, Turkey: Influence of orogen-normal collision vs. wrench-dominated tectonics on p–t–t paths. *Journal of Metamorphic Geology*, *19*(4), 411–432. https://doi.org/10.1046/j.0263-4929.2001.00319.x

Zeng, Q., Lin, F.-C., & Tsai, V. C. (2024). Spurious Rayleigh-wave apparent anisotropy near major structural boundaries: A numerical and theoretical investigation. *Geophysical Journal International*, *239*(2), 901–913. https://doi.org/10.1093/gji/ggae305

Zhang, S., Feng, L., & Ritzwoller, M. H. (2020). Three-station interferometry and tomography: Coda versus direct waves. *Geophysical Journal International*, *221*(1), 521–541. https://doi.org/10.1093/gji/ggaa046

Zhang, S., & Karato, S. I. (1995). Lattice preferred orientation of olivine aggregates deformed in simple shear. *Nature*, *375*(6534), 774–777. https://doi.org/10.1038/375774a0

Zhang, S., Wang, H., Wu, M., & Ritzwoller, M. H. (2021). Isotropic and azimuthally anisotropic Rayleigh wave dispersion across the Juan de Fuca and Gorda plates and U.S. Cascadia from earthquake data and ambient noise two- and three-station interferometry. *Geophysical Journal International*, *226*(2), 862–883. https://doi.org/10.1093/gji/ggab142

References From the Supporting Information

Beck, S., & Zandt, Z. (2005). Continental lithospheric deformation along a major strike-slip fault zone: The central North Anatolian fault zone, Turkey [Dataset]. *International Federation of Digital Seismograph Networks*. https://doi.org/10.7914/SN/YL_2005

Bowman, J. R., & Ando, M. (1987). Shear-wave splitting in the upper-mantle wedge above the Tonga subduction zone. *Geophysical Journal International*, *88*(1), 25–41. https://doi.org/10.1111/j.1365-246x.1987.tb01367.x

Chevrot, S. (2000). Multichannel analysis of shear wave splitting. *Journal of Geophysical Research*, *105*(B9), 21579–21590. https://doi.org/10.1029/2000JB900199

DANA. (2012). Dense array for North Anatolia [Dataset]. *International Federation of Digital Seismograph Networks*. https://doi.org/10.7914/SN/YH_2012

Disaster and Emergency Management Authority. (1990). Turkish national seismic network [Dataset]. *International Federation of Digital Seismograph Networks*. https://doi.org/10.7914/SN/TU

Efron, B. (1979). Bootstrap methods: Another look at the jackknife. *Annals of Statistics*, *7*(1). https://doi.org/10.1214/aos/1176344552

Ergintav, S., Comoglu, M. & Ozel, N. M. (2013). MARsite project [Dataset]. *International Federation of Digital Seismograph Networks*. https://doi.org/10.7914/SN/6G_2013

Friederich, W., & Meier, T. (2005). Egelados project 2005/07, RUB bochum, Germany [Dataset]. *Deutsches GeoForschungsZentrum GFZ*. https://doi.org/10.14470/M87550267382

Geological Survey Department Cyprus. (2013). Cyprus broadband seismological network [Dataset]. *International Federation of Digital Seismograph Networks*. https://doi.org/10.7914/SN/CQ

GFZ Potsdam, & BU-Kandilli. (2006). Prince Islands real-time earthquake monitoring system [Dataset]. *International Federation of Digital-Seismograph Networks*. https://doi.org/10.7914/SN/PZ

GEOFON Data Centre. (1993). GEOFON seismic network [Dataset]. *Deutsches GeoForschungsZentrum GFZ*. https://doi.org/10.14470/TR560404

Kandilli Observatory and Earthquake Research Institute, Boğaziçi University. (2013). Istanbul university seismic network [Dataset]. *International Federation of Digital Seismograph Networks*. https://www.fdsn.org/networks/detail/IJ/

Kandilli Observatory and Earthquake Research Institute, Boğaziçi University. (1971). Kandilli observatory and earthquake research Institute (KOERI) [Dataset]. *International Federation of Digital Seismograph Networks*. https://doi.org/10.7914/SN/KO

Kennett, B. L. N., Engdahl, E. R., & Buland, R. (1995). Constraints on seismic velocities in the Earth from traveltimes. *Geophysical Journal International*, *122*(1), 108–124. https://doi.org/10.1111/j.1365-246X.1995.tb03540.x

Ilia State University- Seismic Monitoring Centre of Georgia. (1988). National seismic network of Georgia [Dataset]. *International Federation of Digital Seismograph Networks*. https://doi.org/10.7914/1yx9-8844

Laske, G., Masters, G., Ma, Z., & Pasyanos, M. (2013). Update on CRUST1.0 – A 1-degree global model of Earth's crust. *Geophysical Research Abstracts*, *15*.

Liu, C., Yao, H., Yang, H., Shen, W., Fang, H., Hu, S., & Qiao, L. (2019). Direct inversion for three-dimensional shear wave speed azimuthal anisotropy based on surface wave ray tracing: Methodology and application to Yunnan, Southwest China. *Journal of Geophysical Research: Solid Earth*, *124*(11), 11394–11413. https://doi.org/10.1029/2018jb016920

Liu, C., & Ritzwoller, M. H. (2024). Seismic anisotropy and deep crustal deformation across Alaska. *Journal of Geophysical Research: Solid Earth*, *129*(5), e2023JB028525. https://doi.org/10.1029/2023jb028525

Montagner, J. P., & Nataf, H. C. (1986). A simple method for inverting the azimuthal anisotropy of surface waves. *Journal of Geophysical Research*, *91*(B1), 511–520. https://doi.org/10.1029/JB091iB01p00511

Montagner, J.-P., & Anderson, D. L. (1989). Petrological constraints on seismic anisotropy. *Physics of the Earth and Planetary Interiors*, *54*(1–2), 82–105. https://doi.org/10.1016/0031-9201(89)90189-1

National Observatory of Athens, Institute of Geodynamics. (1975). Hellenic seismic network [Dataset]. *International Federation of Digital Seismograph Networks*. https://doi.org/10.7914/SN/HL

Paul, A., & Karabulut, H., & RESIF. (2007). Seismic network XW:SIMBAAD temporary experiment - Anatolia Western transect (RESIF-SISMOB). *RESIF - Réseau Sismologique et géodésique Français*. https://doi.org/10.15778/RESIF.XW2007

Paul, A., & Karabulut, H., & RESIF. (2008). Seismic network YI:SIMBAAD temporary experiment - Anatolia Eastern transect (RESIF-SIS-MOB). *RESIF - Réseau Sismologique et géodésique Français*. https://doi.org/10.15778/RESIF.YI2008

Paul, A., & Karabulut, H., & RESIF. (2013). Seismic network XY:SIMBAAD temporary experiment - backbone of broadband stations. *RESIF - Réseau Sismologique et géodésique Français*. https://doi.org/10.15778/RESIF.XY2007

Sandvol, E. (2013). Continental dynamics/Central Anatolian Tectonics: Surface to mantle dynamics during collision to escape [Dataset]. *International Federation of Digital Seismograph Networks*. https://doi.org/10.7914/SN/YB_2013

Silver, P. G., & Chan, W. W. (1991). Shear wave splitting and subcontinental mantle deformation. *Journal of Geophysical Research*, *96*(B10), 16429–16454. https://doi.org/10.1029/91jb00899

Technological Educational Institute of Crete. (2006). Seismological network of Crete [Dataset]. *International Federation of Digital Seismograph Networks*. https://doi.org/10.7914/SN/HC